

Supporting Information

Giant Enhancement in Radiative Heat Transfer in Sub-30 nm Gaps of Plane Parallel Surfaces

Anthony Fiorino¹, Dakotah Thompson¹, Linxiao Zhu¹, Bai Song¹, Pramod Reddy^{1,2,*}, and
Edgar Meyhofer^{1,*}

¹Department of Mechanical Engineering, University of Michigan, Ann Arbor, MI 48109, USA

²Department of Materials Science and Engineering, University of Michigan, Ann Arbor, MI
48109, USA

* email: pramodr@umich.edu

* email: meyhofer@umich.edu

1. Experimental Methods

Parallelization of emitter and receiver. Parallelization of the emitter and receiver devices is a two-stage process. In the first stage, which we call “coarse parallelization,” we use an optical microscope objective (Zeiss LD EC Epiplan-Neofluar 50×/0.55 HD) with a shallow depth of field (2 μm) to image a region of the receiver chip. By bringing a particular region of the chip into focus, we can determine its relative z -position to within ~ 2 μm . Using our nanopositioner to tip and tilt the receiver until all areas of the chip are simultaneously in focus, we can achieve planarity to within 2 μm across the ~ 1 cm length of the receiver chip. This parallelism translates to a maximum angular deviation of ~ 200 μrad , or a ~ 10 nm deviation across the 50 μm active area length. We use our microscope objective and nanopositioner to repeat the same process with the emitter chip, which is ~ 8 mm in extent (~ 250 μrad deviation, or 13 nm across the 50 μm mesa length). Thus, it is in principle possible to achieve effective gap sizes as small as ~ 23 nm (estimated using 10 nm receiver deviation \pm 13 nm emitter deviation) using coarse parallelization alone; in practice, however, the emitter mesa is not perfectly parallel to the rest of the emitter chip, probably due to residual stresses in the beams after fabrication. In order to truly reach gap sizes of ~ 25 nm, additional alignment is required.

The second stage of the alignment process, which we call “fine parallelization,” is predicated on the idea that, for a given gap size, the radiative heat flux between perfectly planar surfaces is maximized when those planes are perfectly parallel, and is reduced for imperfect alignment. Based on this idea, we displaced the receiver towards the emitter and noted the radiative heat flux immediately prior to contact. We then used our nanopositioner to tip or tilt the emitter in steps of ~ 120 μrad before initiating another contact, again recording the radiative heat flux immediately prior to contact. By iterating on this approach until an optimum in heat flux was

obtained, we estimate a maximum deviation from parallelism of ~ 120 μrad per rotation axis, or ~ 12 nm across the 50 μm active area (2 axes $\times 150$ $\mu\text{rad} \times 50$ μm).

Optical detection of mechanical contact between emitter and receiver. To detect mechanical contact between the emitter and receiver, we use a laser deflection scheme similar to that employed in atomic force microscopes. As schematically illustrated in Fig. 2b, we focused a laser onto the backside of the suspended emitter device and subsequently focused the reflected beam onto a two-piece segmented photodiode. When the receiver chip makes mechanical contact with the emitter device, the relatively compliant emitter device is displaced upwards, causing a sudden change in the difference in output of the two detector segments (which we call the “dc contact signal”), as seen in the bottom panel of Fig. 2c. To further confirm that the receiver and emitter are in fact in contact, we also modulated the position of the receiver by ~ 5 nm at 4 kHz and used a lock-in amplifier to monitor the 4 kHz component of the detector difference signal (which we call the “ac contact signal”). As can be seen in the third panel of Fig. 2c, the ac contact signal reads zero when there is a finite vacuum gap separating the emitter and receiver, but when they are in contact the receiver drives the emitter position at 4 kHz such that the locked-in ac signal suddenly jumps.

2. Determination of emitter beam conductance

As can be seen in Eqn. 1 in the main text, calculating the heat flux across the vacuum gap requires knowledge of the thermal conductance G_{beam} of the emitter suspension beams. Because we use a sinusoidal current to determine G_{beam} , we also require the thermal time constant of the emitter device, as explained below.

Emitter microdevice thermal frequency response. We use a modulation based approach¹ to measure the temperature rise of our emitter island due to a sinusoidal heat input. We drive an

alternating current with amplitude I_{1f} and frequency f through the Pt heater/thermometer on the emitter island. The sinusoidal current drives a sinusoidal temperature rise with amplitude ΔT_{2f} and frequency $2f$. A voltage component at frequency $3f$ develops across the Pt heater/thermometer according to $V_{3f} = \frac{I_f \alpha_0 \Delta T_{2f} R_0}{2}$, where $R_0 = 3123 \Omega$ is the electrical resistance and $\alpha_0 = 2.03 \times 10^{-3} \text{ K}^{-1}$ is the temperature coefficient of electrical resistance of the Pt heater/thermometer, each at the reference temperature (300 K). We measured the voltage V_{3f} with a custom-built circuit and lock-in amplifier over a range of frequencies f , as seen in Fig. S1a. It can be seen in Fig. S1a that for $2f > 5 \text{ Hz}$, the V_{3f} signal rolls off because of the thermal time constant of the emitter device. We thus chose $2f = 2 \text{ Hz}$ to measure the thermal conductance of the beams, so that the attenuation was not more than 3%.

Emitter microdevice beam thermal conductance. In the absence of near-field radiative heat transfer to the receiver device, heat flow from the emitter island to the environment is dominated by heat conduction through the suspension beams. Thus when we pass current I_{1f} through the Pt heater/thermometer as described above, we use the known power input Q_{2f} and measured sinusoidal temperature oscillations ΔT_{2f} to calculate the beam thermal conductance according to $Q_{\text{in}} = G_{\text{beam}} \times \Delta T_{2f}$. To reduce error, we repeated the measurement for a range of Q_{in} and fit a line to the resulting data (Fig. S1b) to determine $G_{\text{beam}} = 109.8 \mu\text{W/K}$. A 95% confidence interval calculated on the best fit curve indicates an error bound of $\pm 0.8 \mu\text{W/K}$, or less than 1% of the measured signal.

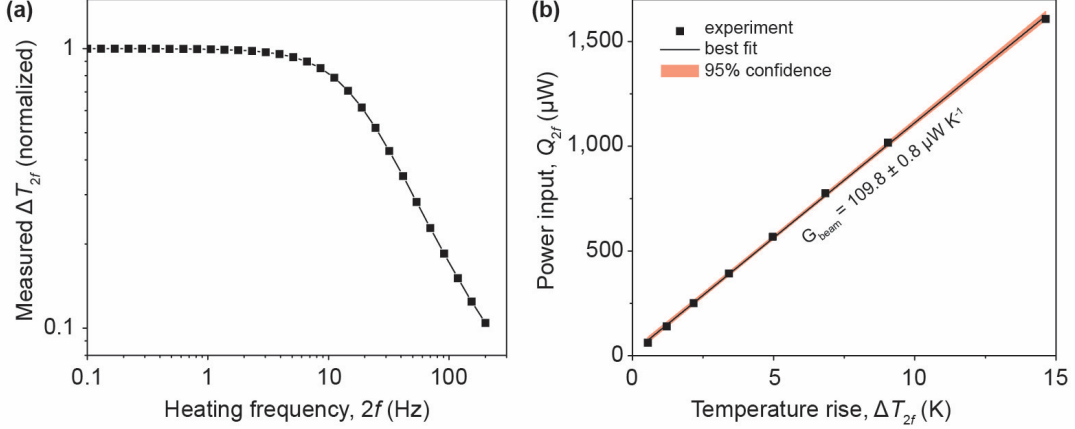


Figure S1. (a) Measured thermal frequency response of our emitter microdevice. The data has been normalized to the low-frequency limit. (b) Power input vs. measured temperature rise for our emitter device in vacuum. The best fit line indicates a beam thermal conductance of $109.8 \mu\text{W K}^{-1}$ and the 95% confidence interval indicates a high degree of certainty.

3. Theoretical modeling of near-field radiation

The thermal radiation model used in this study to predict the near-field radiative heat flux is based on Rytov's fluctuational electrodynamics^{2, 3}. For a 1-dimensional, 2-body system composed of 5 layers (2 emitter layers, 1 vacuum gap layer, 2 receiver layers, as in Fig. 2b in the main text), we calculate the radiative heat flux $q_{01 \rightarrow 34}$ from layers 0 and 1 to layers 3 and 4 according to

$$q_{01 \rightarrow 34} = \int_0^\infty \frac{d\omega}{4\pi^2} [\Theta(\omega, T_H) - \Theta(\omega, T_L)] \int_0^\infty dk \cdot k \cdot [\tau^s(\omega, k) + \tau^p(\omega, k)] \quad (\text{S1})$$

where ω is the angular frequency, $\Theta(\omega, T) = \frac{\hbar\omega}{e^{\hbar\omega/k_B T} - 1}$, $T_{H(L)}$ is the emitter (receiver) temperature,

k is component of the wavevector parallel to the layers, and $\tau^{s(p)}$ is the transmission term associated with photons with s-(p)-polarization. The transmission terms can be calculated according to

$$\tau^{\alpha=s,p}(\omega, k) = \begin{cases} \frac{(1-|\rho_{20}^\alpha|^2)(1-|\rho_{24}^\alpha|^2)}{|D^\alpha|^2} & \text{if } k < \frac{\omega}{c} \\ \frac{4 \operatorname{Im}(\rho_{20}^\alpha) \operatorname{Im}(\rho_{24}^\alpha) e^{-2\operatorname{Im}(k_{z,2})t_2}}{|D^\alpha|^2} & \text{if } k > \frac{\omega}{c} \end{cases} \quad (\text{S2})$$

where $D^\alpha = 1 - \rho_{20}^\alpha \rho_{24}^\alpha e^{2ik_{z,2}t_2}$ is a Fabry-Perot-like denominator, $k_{z,m} = \sqrt{\varepsilon_m \frac{\omega^2}{c^2} - k^2}$ is the perpendicular component of the wavevector in layer m , t_m is the thickness of layer m , c is the light speed in vacuum, and ρ_{ml} is the total Fresnel reflection coefficient for non-adjacent layers m and l . The latter can be calculated according to

$$\rho_{20}^\alpha = \frac{\rho_{21}^\alpha + \rho_{10}^\alpha e^{2ik_{z,1}t_1}}{1 - \rho_{12}^\alpha \rho_{10}^\alpha e^{2ik_{z,1}t_1}} \quad \text{and} \quad \rho_{24}^\alpha = \frac{\rho_{23}^\alpha + \rho_{34}^\alpha e^{2ik_{z,3}t_3}}{1 - \rho_{32}^\alpha \rho_{34}^\alpha e^{2ik_{z,3}t_3}}. \quad (\text{S3})$$

The Fresnel reflection coefficients for adjacent layers, ρ_{mn} , in Eqn. S3 above can be calculated as

$$\rho_{mn}^s = \frac{k_{z,m} - k_{z,n}}{k_{z,m} + k_{z,n}} \quad \text{and} \quad \rho_{mn}^p = \frac{\varepsilon_n k_{z,m} - \varepsilon_m k_{z,n}}{\varepsilon_n k_{z,m} + \varepsilon_m k_{z,n}}, \quad (\text{S4})$$

where ε_m is the dielectric function for material comprising layer m . For our model, we set $t_1 = t_3 = 2 \mu\text{m}$ and varied the gap size t_2 . Layers 0 and 4 are semi-infinite. Once the geometry of all layers is specified (i.e., all thicknesses t_m are fixed), the only parameter in Eqn. S1 is the dielectric function. For the Si layers (0 and 4), we modeled the dielectric function using a modified Drude model⁴. The dielectric function for the SiO₂ layers (1 and 3) was interpolated from tabulated data⁵.

4. Comparison of measured heat flux enhancement to d^{-2} trendline

Near-field radiative heat transfer between parallel planar surfaces that is dominated by surface phonon polariton modes should in principle be proportional to d^{-2} (where d is the vacuum gap

size). For other geometries besides parallel planes, such as between curved surfaces or tilted plates, the proportionality is given by $d^{-\alpha}$, where $\alpha < 2$ generally. Therefore we expect that plotting our measured heat flux against d^{-2} can yield information about how well our system can be approximated by perfectly flat and parallel planes. In Fig. S2, we plot the same data from Fig. 3a alongside a d^{-2} curve, on logarithmic axes. We find that the d^{-2} line follows our data fairly well for $d < 100$ nm, where surface phonon polaritons begin to dominate. This indicates that our device curvature and deviations from parallelism are quite small.

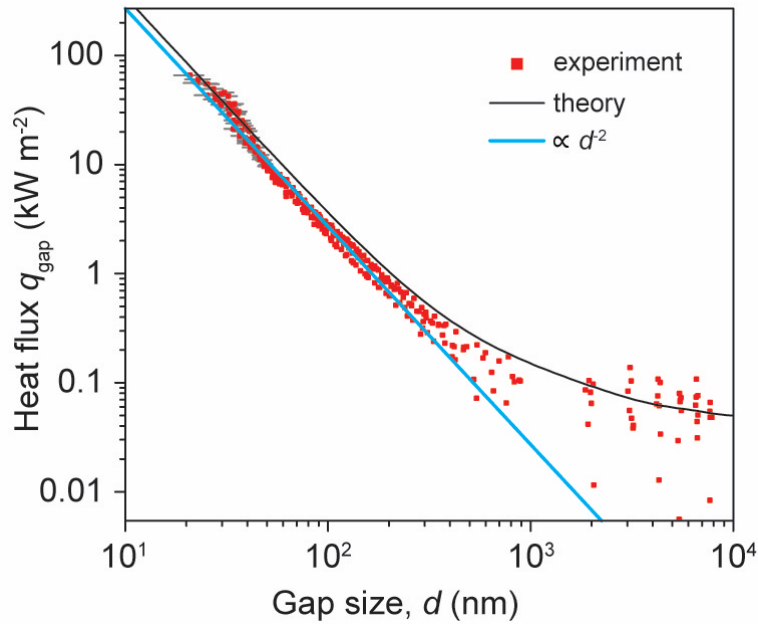


Figure S2. Heat flux vs. gap size. Measured data (red squares), error bars (gray lines), and theoretical expectation (black line) are the same as in Fig. 3a. In addition, a line proportional to d^{-2} has been added for comparison (blue line).

References

1. Cahill, D. G. *Rev. Sci. Instrum.* **1990**, *61*, 802-808.
2. Rytov, S. M.; Kravtsov, I. U. A.; Tatarskii, V. I., *Principles of Statistical Radiophysics 2*. Springer-Verlag: Berlin, **1987**.
3. Narayanaswamy, A.; Zheng, Y. *J. Quant. Spectrosc. & Rad. Trans.* **2014**, *132*, 12-21.
4. Wang, L. P.; Zhang, Z. M. *Nanosc. Microsc. Therm.* **2013**, *17*, 337-348.
5. Palik, E. D., *Handbook of Optical Constants of Solids*. Academic Press: San Diego, **1998**.